Contributions to Geophysics and Geodesy Vol. 55/1, 2025 (49–69)

Principles of imaging subsurface magnetic susceptibility with application to synthetic and field examples

Hassan MOHAMED*

Department of Ground Geophysics, Exploration Division,
Egyptian Nuclear Materials Authority,
P.O. Box 530, Maadi, Cairo, Egypt

Abstract: In this study, a simple new methodology for imaging subsurface magnetic susceptibility from three-dimensional (3-D) correlation tomography of magnetic data is presented. This methodology can be used to rapidly evaluate the equivalent subsurface magnetic susceptibility distribution, especially when powerful commercial programs are unavailable. In correlation tomography, the region of interest is divided into a regular 3-D grid, and the correlation is then calculated between the measured magnetic field data and the computed magnetic field data resulting from a magnetic point dipole. A probabilistic estimate of the distribution of the equivalent magnetic dipoles can be achieved using the correlation coefficient technique. The coefficient values range between -1 and $+1$ and are equivalent physical parameters. The cross-correlation values obtained at different depth intervals are plotted to show that the higher the correlation coefficient, the greater the equivalent magnetic dipole distribution and vice versa. The computer program was tested on both synthetic magnetic data and on real field data acquired over the west Garida and Hamama deposits in Egypt's Eastern Desert. Overall, the cross-correlation tomography approach yields quick, efficient results that can be used as a basis for subsequent in-depth modelling.

Key words: inversion, magnetic method, West Garida, Hamama, Eastern Desert, Egypt

1. Introduction

Aeromagnetic surveys form an important part of the complex of geophysical survey methods with a wide range of uses, with applications ranging from large-scale regional geological mapping to small-scale engineering site investigations to identify pipes and cables in the very near-surface (*Hinze et al., 2013*). The Earth's magnetic field can be approximately represented as a dipole positioned near the Earth's centre that is inclined with regard to the rotational axis (*Griffiths and King, 1981*). Magnetic data surveying is

*corresponding author, e-mail: hassan87mohamed@gmail.com; phone: 002-01003695033

conducted when information about geologic structures, ore body characterization (e.g., location, depth, and magnetic susceptibility), and geotechnical investigations are required. According to *Telford et al. (1990)*, magnetic measurements are among the simplest and least expensive types of geophysical measurements. Historically, line profiles or maps of raw or filtered survey data were used to extract meaningful information from geophysical field observations. These images can be used to estimate the positions and numbers of buried objects; for example, magnetic data maps can be used to show an area's geologic structure or characterize an unusual region that may be connected to a desired target. Unfortunately, while these data maps offer some insights into the lateral variation of the body, they provide little information about the distribution of its physical characteristics at depth. To determine the position and depth of two-dimensional (2-D) geologic boundaries, Euler deconvolution can be applied to estimate the depths and locations of magnetic sources by applying the method to the total field magnetic data without a priori geological information (*Thompson, 1982*). *Nabighian (1972)* proved that geological boundaries and depths to the top of these boundaries can be estimated using the analytic signal method. Recently, combinations of these methods, such as the "AN-EUL" method developed by *Salem and Ravat (2003)*, have been used to facilitate and accelerate the interpretation of magnetic data. *Essa et al. (2024)* introduced approach for modelling magnetic field data collected across vertical and dipping faults.

However, because of the inherent variety of problems encountered in geology, no single geophysical technique works well in all instances. Therefore, in many cases, combining multiple techniques will yield the optimal results. As part of this combination of techniques, geophysical data inversion is widely used, which represents a powerful technique for deriving the subsurface distribution of physical properties from field data (*Williams, 2008*). The subsurface magnetic susceptibility distribution is one of the most important quantitative measures for interpreting an area's geology and represents an important target variable for geophysical inversion (*Essa et al., 2021*).

Magnetic data inversion can be classified into two types according to the target parameter. The classical inversion method discussed by *Fedi et al. (2005)*, *Zhdanov (2002)*, *Li and Oldenburg (1996; 1998)*, and *Pilkington (1997)* involves inverting the magnetic susceptibility directly. This type of inversion takes longer to compute and requires sufficient memory to store

the sensitivity matrix. Additional constraints within a specific range can be introduced to address the problem of non-uniqueness of the source distribution. The second type of magnetic inversion involves the use of correlation tomography. In this approach, the corresponding magnetic dipole distribution is visualized in terms of probability. The efficiency of this method has been demonstrated in previous studies; for example, *Mauriello and Patella (1999a,b)* successfully created probability tomography for the study of geoelectric and electromagnetic approaches, while self-potential data were analysed by *Patella (1997a,b)* and *Mauriello et al. (1998)*.

The analysis of gravity and magnetic data using correlation tomography has been discussed by *Chianese and Lapenna (2007)*, *Guo et al. (2011a,b)*, *Fedi and Pilkington (2012)*, *Liu et al. (2014)*, *Guo et al. (2014)*, and *Mauriello and Patella (2001; 2005; 2008)*.

In this study, we present a novel method for magnetic data inversion based on the principle of correlation coefficients method.

A major advantage of the correlation tomography method presented in the present study over other inversion methods is that this approach allows the subsurface three-dimensional (3-D) magnetic dipole distribution to be rapidly determined. The correlation tomography approach requires little computer memory, the results are readily interpreted, as they range between -1 and +1, and a priori geological information is not required for the tomography process. The remnant magnetization has a little effect on the magnetic field anomaly; the calculated correlation will reduce the effects of remanent magnetization (*Guo et al., 2014*).

The computer code developed in this work was tested on synthetic examples and a field example from the West Garida and Hamama deposits in the Eastern Desert of Egypt.

2. Theory of correlation imaging of magnetic data

2.1. Structure of the magnetic field anomaly

To obtain a magnetic survey, the horizontal coordinate system (x, y) plane is located at sea level, and the vertical axis (z) is typically oriented such that it is positive-downward. The magnetic moment is assumed to be $M_q = J_q\, v_q$ at a point $q(x_q, y_q, z_q)$ in the subsurface, where J_q is the magnetization intensity and v_q is the volume. The magnetization of the dipole is assumed

to have an inclination I and declination A′, while the geomagnetic field is assumed to have an inclination I_0 and declination A'_0.

The following formula can be used to determine the three components of the magnetic field at an observed point (*Hinze et al., 2013; Mohamed et al., 2020*). At a point p at a distance r from the dipole, the scalar magnetic potential is given by:

$$\mathrm{V}(r) = -\left(\frac{\mu_0}{4\pi}\right)\mathbf{m}\cdot\nabla_{\mathrm{p}}\frac{1}{r}\,. \tag{1}$$

The dipole moment m, with magnitude $\mathbf{m} = \mathrm{p}\times l$ (Am^2), $\mathbf{p}$ is the magnitude of either pole, separated by infinitesimal distance l. The dipole moment $\mathbf{m}$ is oriented from the negative pole to the positive pole, r is the distance between the dipole point centre and the observation point P, and $\mu_0 = 4\pi\times 10^{-7}\,\mathrm{NA}^{-2}$, corresponds to the magnetic permeability of air.

The dipole magnetic moment is defined as the combination of the inclination θ_{I} and declination θ_{D} as follows:

$$\begin{aligned}
&\mathbf{m} = \mathbf{m}_x + \mathbf{m}_y + \mathbf{m}_z\,,\\
&\mathbf{m}_x = \mathrm{m}\times(\cos\theta_{\mathrm{I}}\times\sin\theta_{\mathrm{D}})\,\hat{\mathbf{i}}\,,\\
&\mathbf{m}_y = \mathrm{m}\times(\cos\theta_{\mathrm{I}}\times\cos\theta_{\mathrm{D}})\,\hat{\mathbf{j}}\,,\\
&\mathbf{m}_z = \mathrm{m}\times(\sin\theta_{\mathrm{I}})\,\hat{\mathbf{k}}\,,
\end{aligned} \tag{2}$$

The strength of the magnetic moment is defined as m, and the unit vectors in the x, y, and z directions are represented by $\hat{\mathbf{i}}$, $\hat{\mathbf{j}}$, and $\hat{\mathbf{k}}$, respectively.

The vector magnetic field at r is given by:

$$\mathbf{B}_{(x,y,z)} = -\nabla\mathrm{V}(r) = \nabla\left[\left(\frac{\mu_0}{4\pi}\right)\mathbf{m}\nabla_{\mathrm{p}}\frac{1}{r}\right] = \mathrm{B}_x\,\hat{\mathbf{i}} + \mathrm{B}_y\,\hat{\mathbf{j}} + \mathrm{B}_z\,\hat{\mathbf{k}}\,. \tag{3}$$

Hence, the vector magnitude components are given by:

$$\mathrm{B}_x = \frac{3\,\mathrm{C_m}}{r^5}\left[\mathrm{m}_x\left(\Delta x^2 - \frac{r^2}{3}\right) + \mathrm{m}_y(\Delta x\,\Delta y) + \mathrm{m}_z(\Delta z\,\Delta x)\right], \tag{4a}$$

$$\mathrm{B}_y = \frac{3\,\mathrm{C_m}}{r^5}\left[\mathrm{m}_x(\Delta x\,\Delta y) + \mathrm{m}_y\left(\Delta y^2 - \frac{r^2}{3}\right) + \mathrm{m}_z(\Delta z\,\Delta y)\right], \tag{4b}$$

$$\mathrm{B}_z = \frac{3\,\mathrm{C_m}}{r^5}\left[\mathrm{m}_x(\Delta x\,\Delta z) + \mathrm{m}_y(\Delta z\,\Delta y) + \mathrm{m}_z\left(\Delta z^2 - \frac{r^2}{3}\right)\right], \tag{4c}$$

where $C_m = \mu_0/4\pi$, the magnetic vector components are B_x, B_y, and B_z, $\Delta x = x - x_q$, $\Delta y = y - y_q$, and $\Delta z = z - z_q$. Using these components, the dipole source's total magnetic field anomaly for geomagnetic inclination and declination can be calculated using the following equation:

$$B_T(x, y, z) = B_x(\cos\theta_I \cos\theta_D) + B_y(\cos\theta_I \sin\theta_D) + B_z(\sin\theta_I)\,. \tag{5}$$

2.2. Cross-correlation procedure

The imaging approach for the subsurface magnetic dipole is based on the cross-correlation between the magnetic field data measured at the surface and the theoretical magnetic field data calculated by a unit magnetic dipole (scanner dipole). The point dipole is positioned in the centre of the cell of a regular grid, as shown in Fig. 1.

In practice, since the position of the real source generating the anomalous magnetic field is not known. Synthetic source with uniform strength was used to scan the x, y and z half space below the study area, hence the real sources location can be identified in a probabilistic sense.

Using Eq. (5), the magnetic field data can be calculated. After calculating the magnetic field anomaly, the cross-correlation between the computed and measured magnetic fields can then be calculated using Eq. (6). The cross-correlation is calculated from the top to the bottom of the discretized volume.

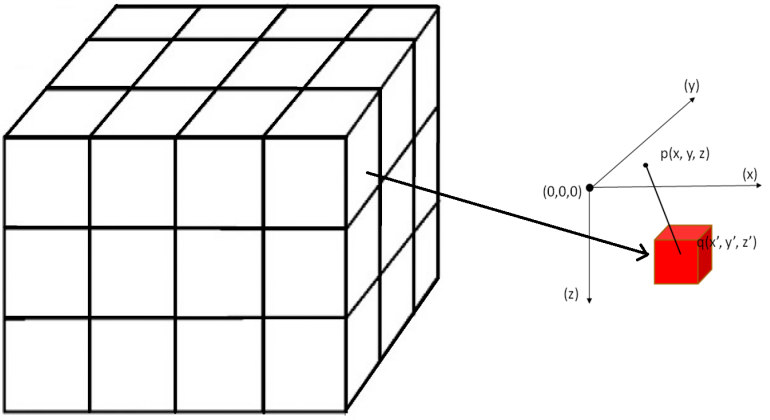

Fig. 1. The mesh used to discretize the study area.

The correlation coefficient function for the computed and observed magnetic field data can be calculated as follows:

$$\mathrm{C}_{\mathrm{TM},q} = \frac{\sum\limits_{i=1}^{N_s} \mathrm{TM}(x_i, y_j, z_k)\, \mathrm{TM}_q(x_i, y_j, z_k)}{\sqrt{\sum\limits_{i=1}^{N_s} \mathrm{TM}^2(x_i, y_j, z_k) \sum\limits_{i=1}^{N_s} \mathrm{TM}_q^2(x_i, y_j, z_k)}}, \tag{6}$$

which satisfies the condition:

$$-1 \leq \mathrm{C}_{\mathrm{TM},q} \leq 1.$$

Here, the number of the observed stations is N_s, and $\mathrm{TM}(x_i, y_j, z_k)$ is the measured field with Cartesian coordinates (x_i, y_j, z_k). Similarly, the calculated magnetic field anomaly at stations (x_i, y_j, z_k) is expressed as $\mathrm{TM}_q(x_i, y_j, z_k)$. We assume that the magnetic dipole moment of a point in our calculation is the same (e.g., $\mathbf{m}_q = 1$). The results of Eq. (6) represent the probability that a magnetic dipole at point q under the surface will form and be the source of the overall magnetic field anomaly observed at the surface. The results from Eq. (6) are then plotted as a 2D map. The correlation imaging ($\mathrm{C}_{\mathrm{TM},q}$) values in Eq. (6) range from -1 to 1, where lower correlation coefficient values indicate anti-correlation between measured and calculated magnetic field anomaly, i.e., a reduced likelihood of a magnetic dipole located in this area, and higher $\mathrm{C}_{\mathrm{TM},q}$ values indicate strong correlation between measured and computed magnetic field data, i.e., a higher likelihood of a magnetic dipole located in this area.

Equation (6) can therefore be used to perform probabilistic estimation of the magnetic susceptibility's 3D subsurface distribution. As the subsurface magnetic susceptibility distribution is imaged using the degree of cross-correlation (Eq. (6)) between the calculated and measured magnetic field data, this technique is known as correlation tomography imaging. As shown in Fig. 1, the region of interest in this work is discretized into a regular 3-D grid.

The output of the method given in Eq. (6) does not provide information about the magnetic susceptibility values directly but instead gives an estimate of the depth to the magnetized sources. Correlation coefficients method doesn't provide evidence of causation and should be used in conjunction with other types of interpretation techniques.

The cross-correlation results can be visualized in either 2-D or 3-D; hence, the subsurface magnetic susceptibility distribution can be described based on the correlation tomography method. In the next part of this work, various theoretical data are tested to simulate the presence of magnetic dipoles at different locations.

3. Synthetic example

The correlation imaging approach is tested here using various synthetic magnetic data. The first synthetic model is a basic geological model of a 3-D magnetized prism hosted in a homogeneous, insensitive half-space. The magnetic intensity of the buried body is assumed to be 10 A/m. Figure 2 shows the configuration of the model, which can be approximated as a point dipole centred at (5000 m, 5000 m and 500 m).

The code to calculate the synthetic data can be written in Fortran 95 as follows:

Location of magnetic dipole

```
   mloc(1)=5000.0d0 !x
   mloc(2)=0.0d0    !y
   mloc(3)=-500.0d0 !z :depth
```

Calc. observed data

```
    p(2)=0.0d0 !Yp
    p(3)=0.0d0 !Zp
    do i=1,21
      p(1)=real (i-1, kind(0d0))*500.0d0 !xp
      gmx=bx (p, mloc, mdip) !Bx
      gmy=by (p, mloc, mdip) !By
      gmz=bz (p, mloc, mdip) !Bz
      gmt=gmx*cos(inc)*cos(dec)+gmy*cos(inc)*sin(dec)+gmz*sin(inc) !Bt
      obs(i)=gmt
!     write(6,*) i, obs(i)
    enddo
```

The magnetic data calculated at the surface extend from 0 to 10,000 m in both horizontal directions, with a grid interval of 500 m and a line spacing of 1000 m; thus, the area of interest is discretized with cell dimensions 500 m, 1000 m and 500 m along the x, y, and z axes, respectively. The model's magnetization and ambient field are assumed to share the same inclination and declination, which are 90 degrees and 0 degrees, respectively. The tomo-

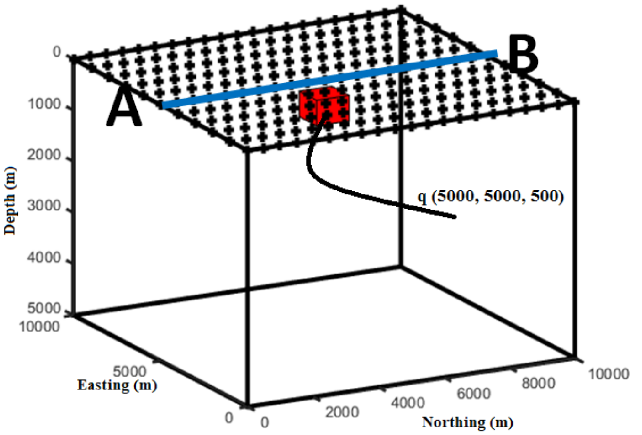

Fig. 2. Three-dimensional visualization of the synthetic model approximated at dipole point (5000 m, 5000 m and 500 m).

space is scanned in a series of horizontal slices, with a depth separation of 500 m from the model's top (0 m) to its base (5000 m).

Magnetic susceptibility values can be estimated by multiplying a small magnetic susceptibility value by the correlation coefficient result (*Guo et al., 2014*). Figures 3a and 3b show observed magnetic anomaly a long profile AB (Fig. 2) compared to the correlation coefficient result multiplied by a certain susceptibility value. Figure 3a shows correlation coefficient result multiplied by 0.09 susceptibility value, the modelling curve has the same trend as the observed data. Figure 3b can show a magnetic susceptibility value (0.1) that can increase the agreement between original and correlation coefficient curve.

Figure 3c shows the output results of Eq. (6) corresponding to each depth interval. The correlation factor calculated at a depth of 500 m is equal to 1, whereas the value calculated at 5000 m is equal to 0.4.

As shown in Fig. 3c, the maximum correlation coefficient is obtained at a depth of 500 m and an x-coordinate of 5000 m, with a steady decrease in the correlation coefficient observed at depths further from the true location of the source body. The correlation imaging maps along profile A–B for the calculated total magnetic field data are displayed in Figs. 4a and 4b.

The true location of the buried magnetized body is clearly identified by using the cross-correlation tomography imaging method. To counteract the

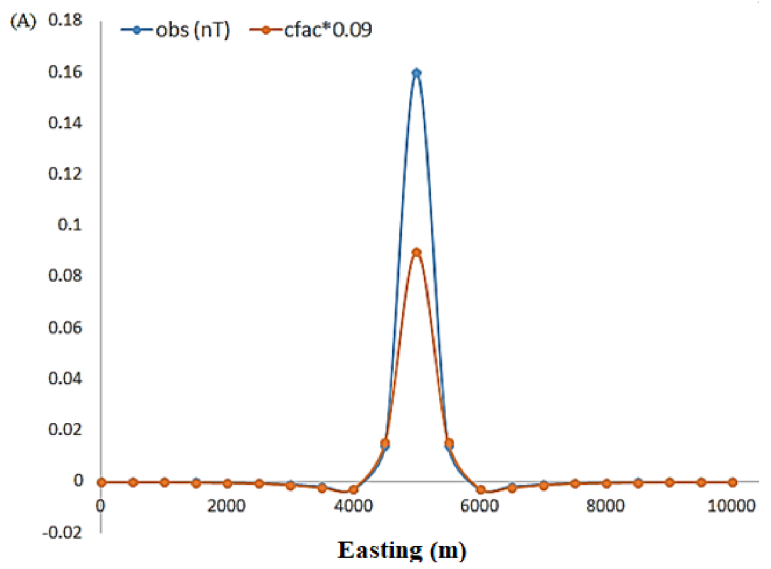

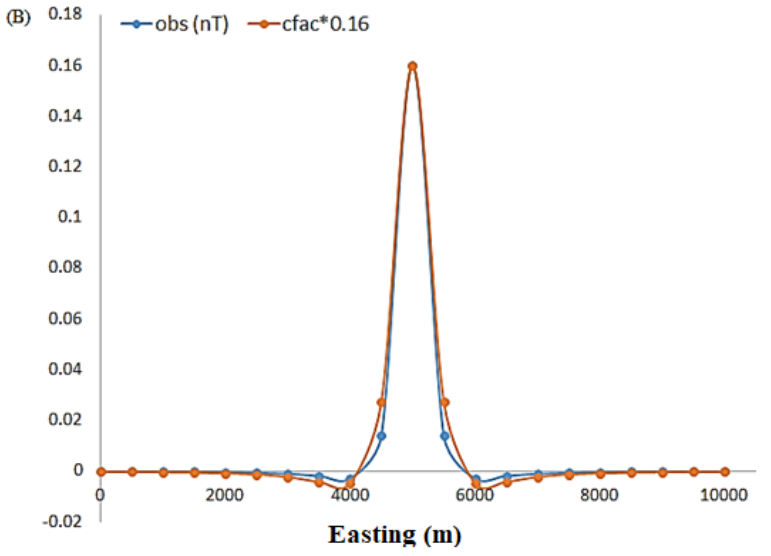

Fig. 3. Continued on the next page.

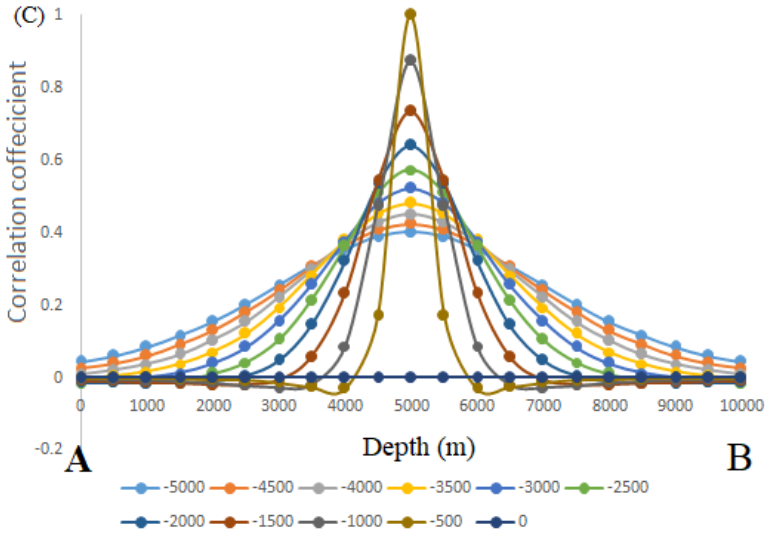

Fig. 3. (a) Observed magnetic anomaly profile compared to correlation coefficient result multiplied by 0.09. (b) Observed magnetic anomaly profile compared to correlation coefficient result multiplied by 0.1. (c) Correlation coefficient values for different depth intervals.

broad range of magnetic susceptibility values (long tail in Fig. 4a), a cutoff of 0.6 was applied to the imaging results (Fig. 4b). As shown, the magnetic source distribution can be effectively identified at the same location as shown by a solid black line.

To test the ability of the correlation tomography approach to isolate two sources, the same parameters were used but with two synthetic models combined in one region (Fig. 5a). One source body A was centred at (0, 0, 100), and a second source body B was centred at (500, 0, 100). As shown, the correlation coefficient results effectively distinguish the two closely spaced prisms (Fig. 5b), with effectively separated source distributions related to the two prisms (Figs. 5c and 5d).

4. Field data

The developed code was tested to obtain the magnetic susceptibility distribution by performing an inversion of geomagnetic field data. This inversion approach was applied to investigate the magnetic field anomalies close

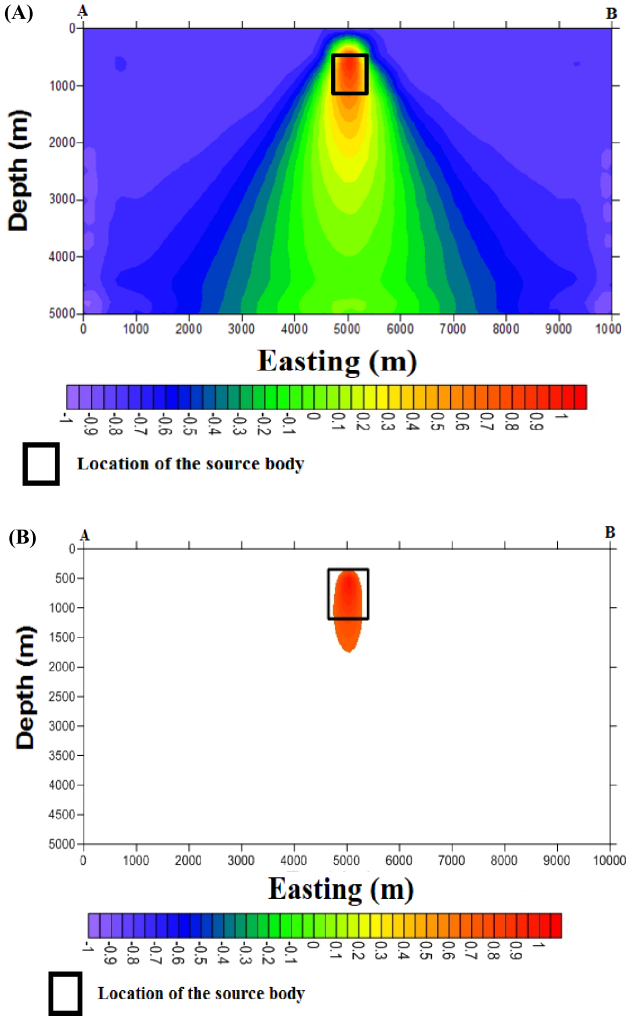

Fig. 4. (a) Results showing the imaged source distribution (susceptibility). (b) Tomography imaging results using a cutoff value at 0.6.

to Hamama and West Garida in Egypt's Eastern Desert. Figure 6 shows the location map of the study area, which lies within the latitude range 26°19′ N – 26°51′ N and longitude range 33°19′ E – 33°45′ E. This study area has high importance due to its gold resource potential and the occurrence of base metals in this region (*Klemm and Klemm, 2013*).

A proton magnetometer with a resolution of 0.01 nT was used to acquire the aeromagnetic measurements at a terrain clearance of 120 m. The data were exported in (x, y, z) form once they had been corrected for the effects of diurnal variation and the International Geomagnetic Reference Field. The magnetic field data were then reduced to the pole (RTP) using an average inclination of 34° and a declination of 2.7° (*Baranov, 1957*).

Figure 7 shows the RTP aeromagnetic data. These data are characterized by both low and high magnetic anomalies over the study area, with

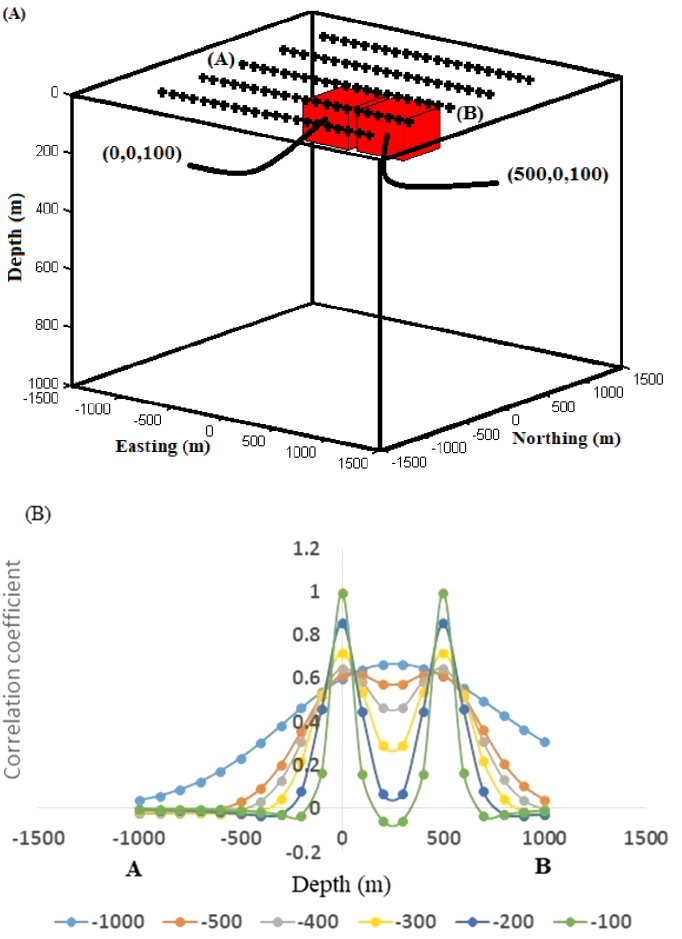

Fig. 5. Continued on the next page.

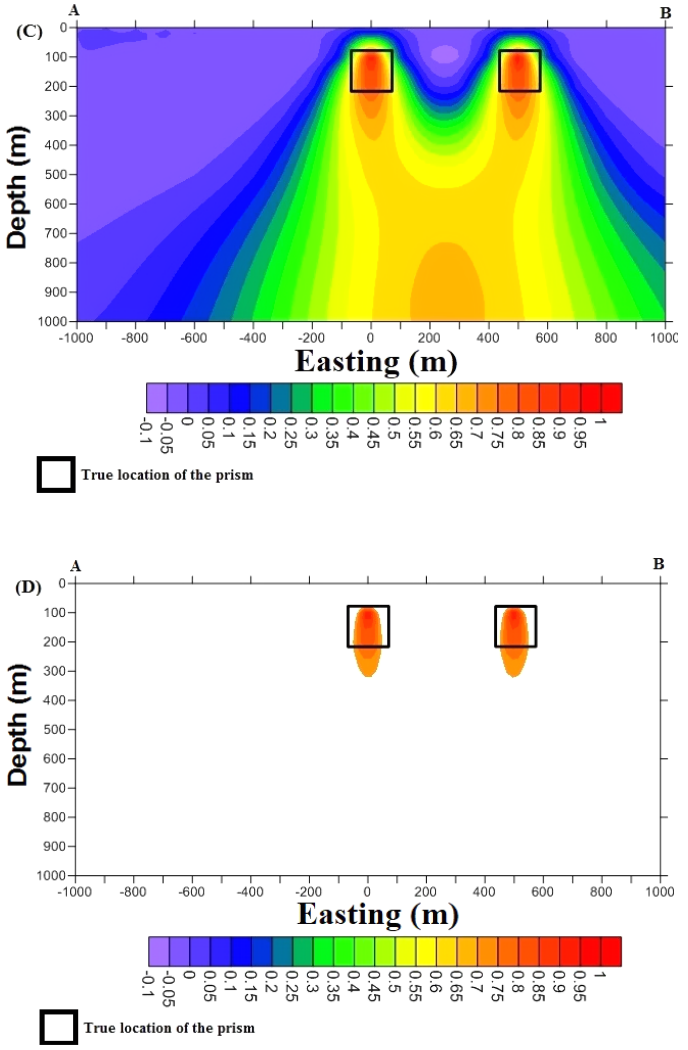

Fig. 5. (a) Three-dimensional visualization of two synthetic models approximated at dipole points (0 m, 0 m and 100 m) and (500 m, 0 m and 100 m). (b) The correlation imaging results along the x-axis, showing a good correlation with the true locations of the two prisms. (c) The imaged source distributions of the two synthetic models approximated at dipole points (0 m, 0 m and 100 m) and (500 m, 0 m and 100 m). (d) Tomography imaging results using a cutoff value of 0.6.

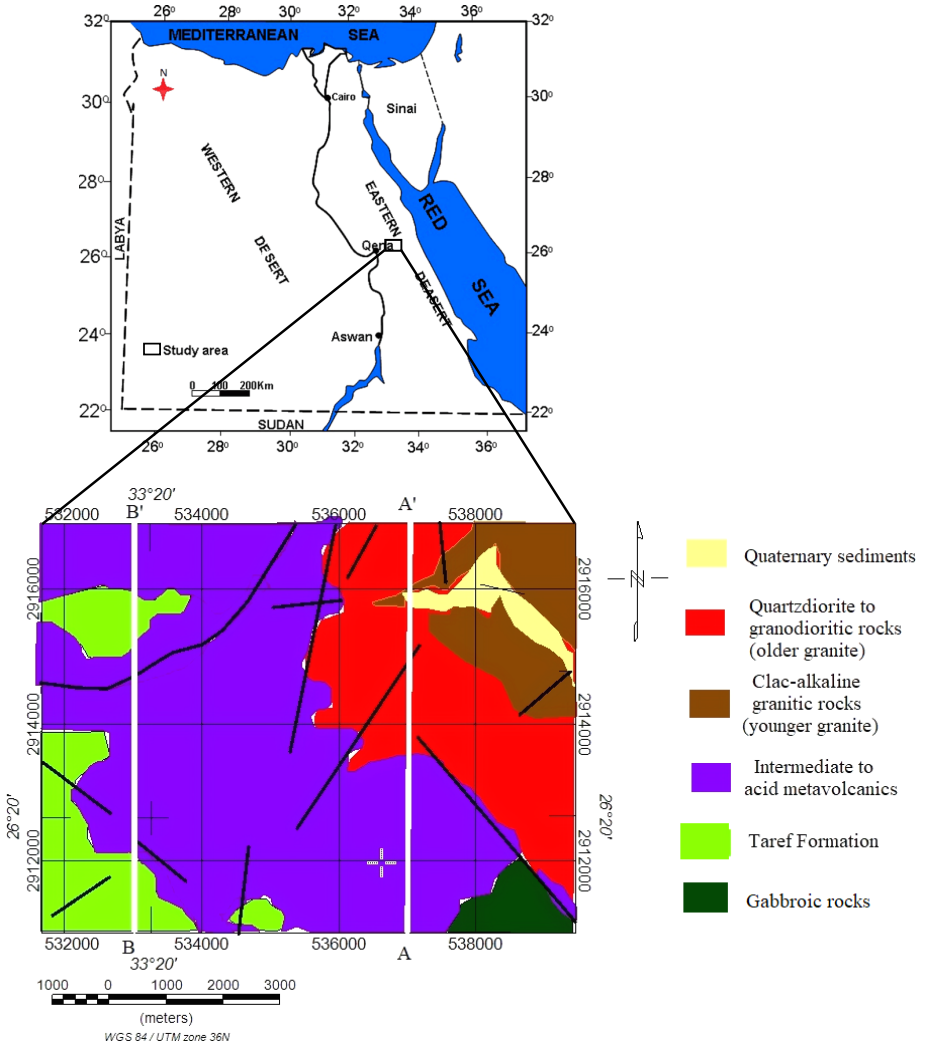

Fig. 6. Location map of the study area (west Garida and Hamama, Eastern Desert, Egypt).

high-amplitude, elongated magnetic anomalies associated with metavolcanic rocks. High susceptibilities are typical for these rock types (*Saad, 1969*). In contrast, the older granitoids and wadi deposits are characterized by low magnetic susceptibilities.

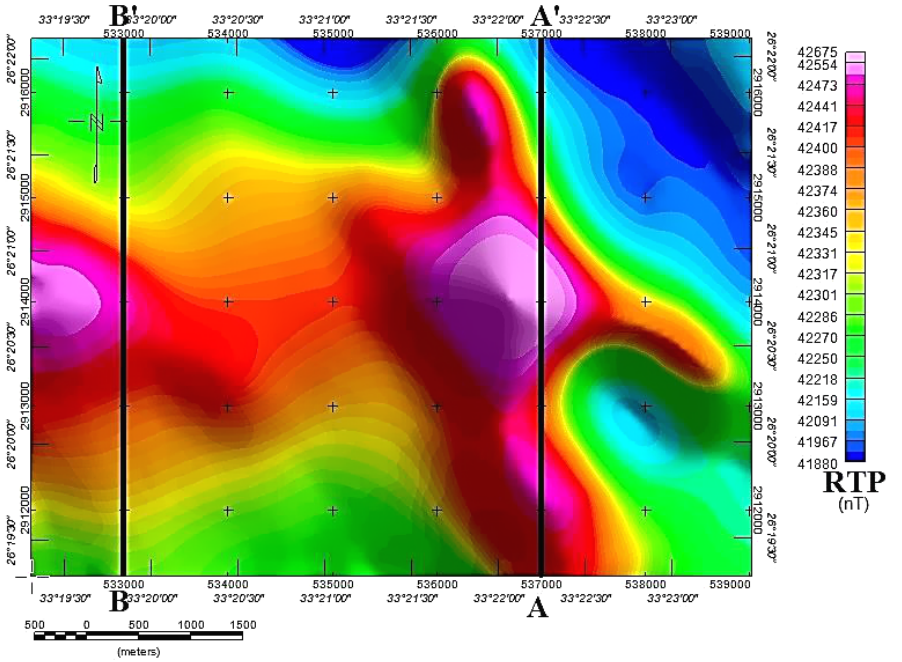

Fig. 7. RTP aeromagnetic data of area west Garida and Hamama, North Eastern Desert, Egypt. The locations of magnetic anomaly profiles A–A′ and B–B′ are shown as black lines.

In this section, the 3-D forward modelling of the magnetic effects (induced magnetization) of a hexahedral (trilinear) prism was calculated by using the Gauss–Legendre quadrature method (GLQ) (*Mohamed et al., 2020*). 3-D forward modelling was used to characterize the study area's subsurface structure. By changing the magnetization and coordinates of the source bodies, Fig. 8a shows the computed magnetic field data, while the 3-D simplified model is shown in Fig. 8b. These figures show good agreement—the higher values in regions 1 and 2 reflect the susceptibility contrast and depth variation in this area. The depths to the magnetized sources ranges from 0.5 to 1.5 km at the western boundary and from approximately 0.7 to 1.5 km in the central portion of the studied area, with magnetization intensities varying from 47 to 59 A/m.

Figure 8b shows a 3-D model for the study area. The model covers 6395 m and 4973 m in the E–W and N–S directions, respectively.

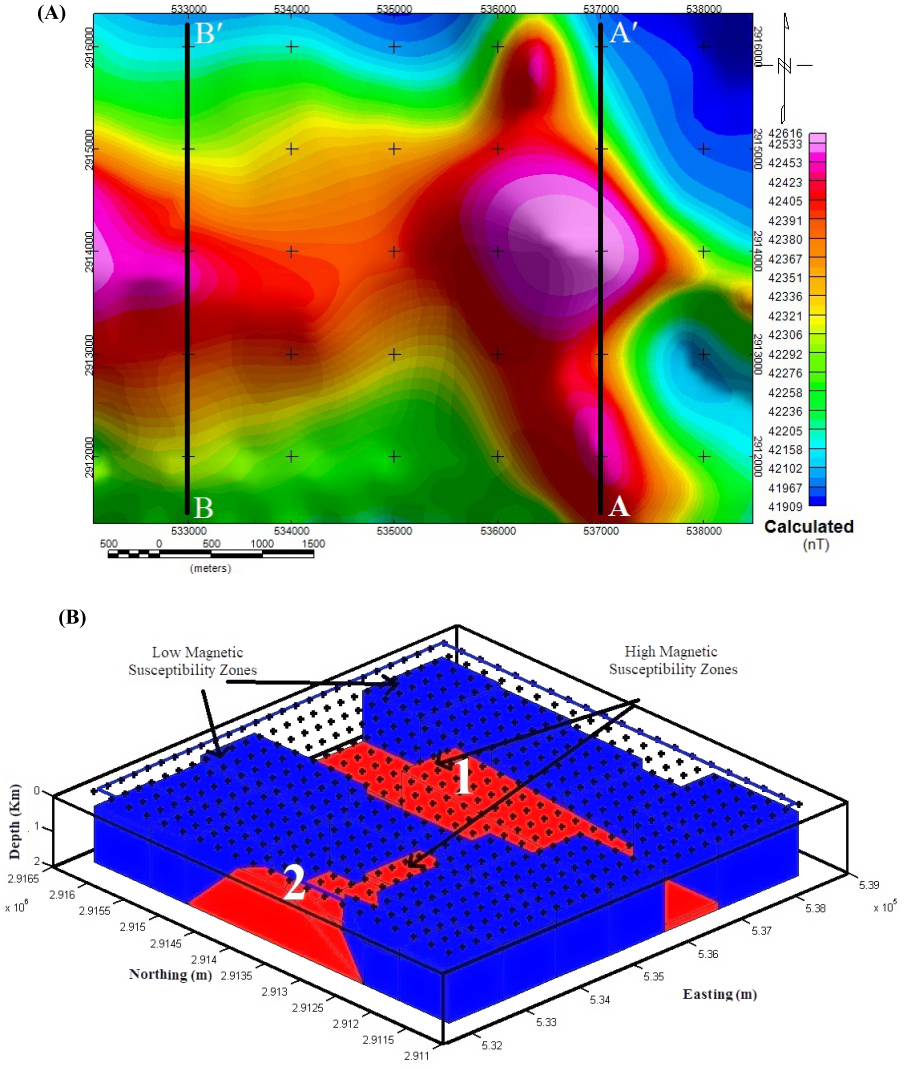

Fig. 8. (a) Image showing the calculated magnetic field data. (b) 3-D simplified model constructed to represent the measured aeromagnetic data.

Overall, a good general agreement with the original aeromagnetic field data can be observed on Figs. 7 and 8a. In addition, Figs. 9a and 9b show a comparison between the measured and calculated magnetic anomaly along

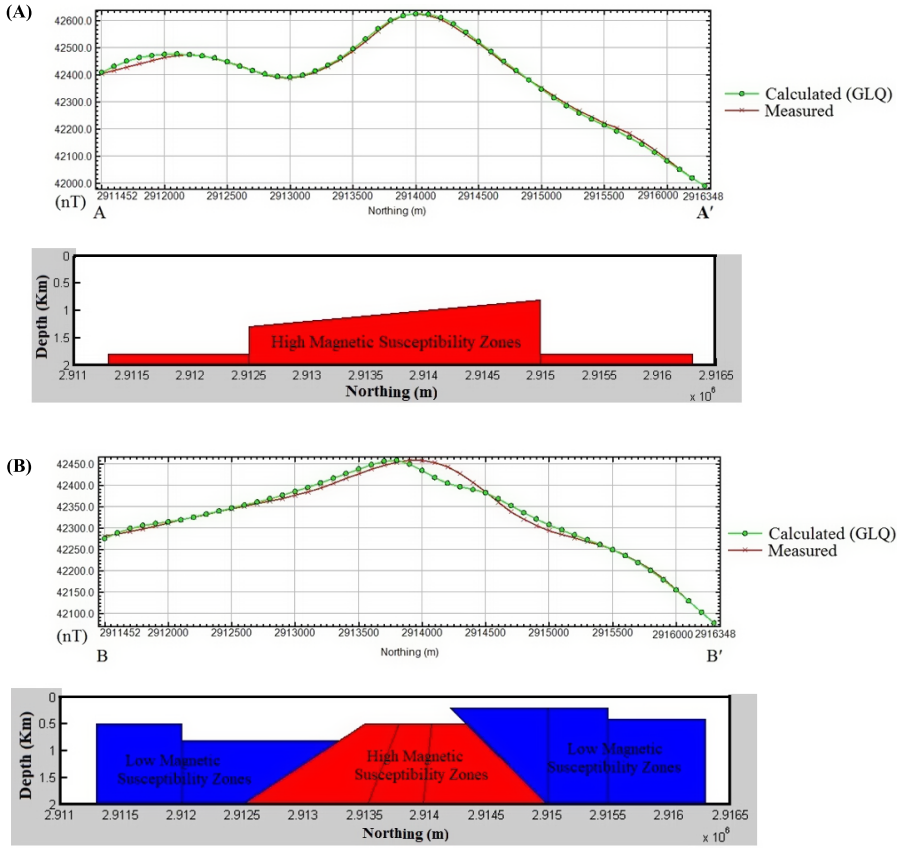

Fig. 9. (a) Magnetic anomaly profile across the main magnetic source along the line A–A′. (b) Magnetic anomaly profile across the main magnetic source along the line B–B′.

two profiles (533000 A–A′ and 537000 B–B′, Fig. 7) across the main magnetic anomaly.

In this section, the cross-correlation is calculated on the RTP magnetic anomaly using Eq. (6). The estimated depth extends from 0 to −2000 m, with a scanning depth interval of 200 m. Figs. 10a and 10b show the imaging results along two profiles (A–A′ and B–B′) crossing the area's main geological structure.

As shown, the high magnetic susceptibility zones coincide with the location of metavolcanic rocks, whereas the low magnetic susceptibility zones

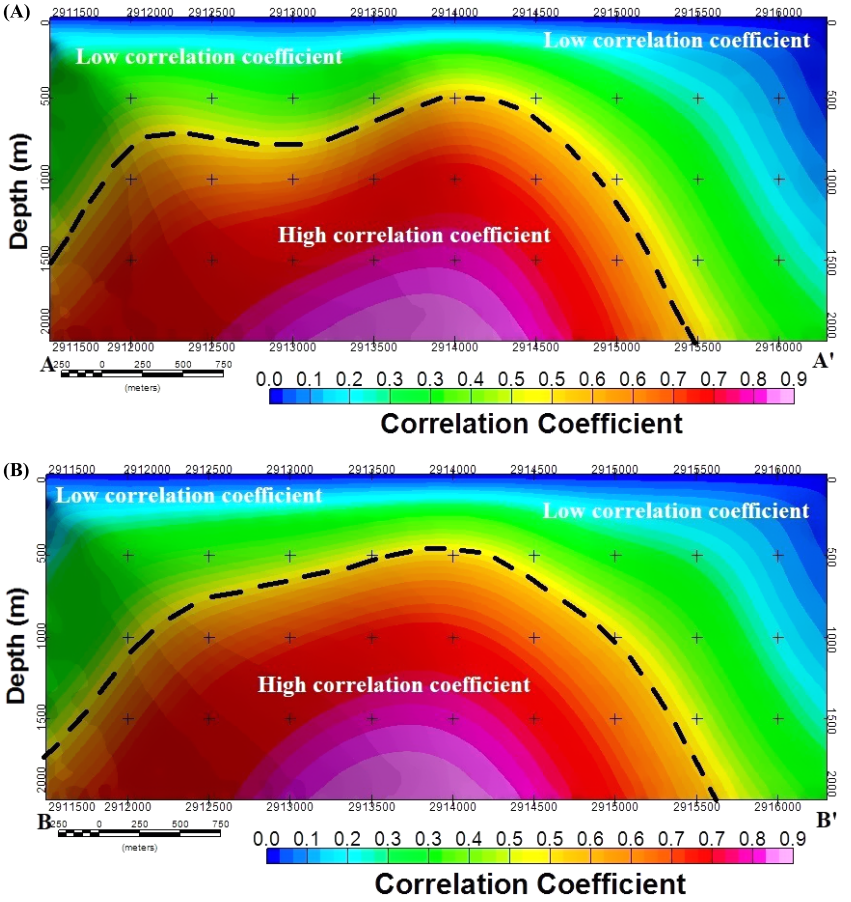

Fig. 10. (a) Profile A–A′ showing the dipole distribution obtained from correlation imaging of the RTP magnetic data. (b) Profile B–B′ showing the dipole distribution obtained from correlation imaging of the RTP magnetic data.

coincide with Wadi sediments and younger granitoid rocks discovered at the surface. Similarly, the high correlation results indicate a high probability of the presence of a magnetized body, whereas the low correlation results indicate the presence of shallow Wadi sedimentary deposits. Overall, the correlation tomography method's results are verified here based on their similarity with the 3-D forward model and known geology in the studied region.

5. Conclusion

In this study, a correlation imaging approach is presented to recognize the most probable occurrence of magnetic dipole accumulation. The sampling interval of the field measurements determines the resolution of the correlation tomography data, with higher imaging resolution achieved with denser data observations. The normalized measure of the degree of correlation between the calculated and measured magnetic field data is represented by correlation coefficient values. Its values range between -1 and $+1$, with a value of 0 implying no correlation. The resulting cross-correlation map can be interpreted using this method to represent the subsurface distribution and probability density of the magnetic sources' positions.

This work's methodology can be used to map the distribution of subsurface magnetic sources. The cross-correlation function allows the most probable location of magnetic dipoles to be determined. The program was tested with magnetic field data from West Garida and Hamama deposits from the Eastern Desert in Egypt. The inversion and forward modelling results reveal that low correlation values correspond to Wadi sediments, whereas high correlation values correspond to high-susceptibility metavolcanic rocks. Overall, the application of the proposed method to the field and synthetic data demonstrates a good agreement with the true locations of the source bodies.

In conclusion, the proposed code is simple, easy to use, stable as it requires low computer memory, and insensitive to noise in the magnetic field data. This approach can be applied stably to large-scale magnetic field data. When little or no prior information is available, it is recommended to use the imaging technique proposed here to estimate the distribution of subsurface magnetic sources.

Acknowledgements. The author is grateful to Hakim Saibi, Professor of geophysics from UAEU and Ahmed A. Ammar, emeritus professor of geophysics from Nuclear Materials Authority for reviewing the manuscript. I greatly appreciate the two anonymous reviewers and editors for their constructive comments and encouragement to improve the manuscript.

Data availability. The data that support the findings of this study are available on request from the corresponding author.

Conflict of interest. None of the authors have a conflict of interest to disclose.

Funding. No fund is provided for this research.

References

Baranov V., 1957: A new method for interpretation of aeromagnetic maps pseudo-gravimetric anomalies. Geophysics, **22**, 2, 359–382, doi: 10.1190/1.1438369.

Chianese D., Lapenna V., 2007: Magnetic probability tomography for environmental purposes: test measurements and field applications. J. Geophys. Eng., **4**, 1, 63–74, doi: 10.1088/1742-2132/4/1/008.

Essa K. S., Abo-Ezz E. R., Anderson N. L., Gomaa O. A., Elhussein M., 2024: Magnetic inversion approach for modeling data acquired across faults: various environmental cases studies. Acta Geophys., **72**, 3, 1819–1845, doi: 10.1007/s11600-023-01184-4.

Essa K. S., Mehanee S., Elhussein M., 2021: Magnetic data profiles interpretation for mineralized buried structures identification applying the variance analysis method. Pure Appl. Geophys., **178**, 3, 973–993, doi: 10.1007/s00024-020-02553-6.

Fedi M., Hansen P. C., Paoletti V., 2005: Analysis of depth resolution in potential-field inversion. Geophysics, **70**, 6, A1–A11, doi: 10.1190/1.2122408.

Fedi M., Pilkington M., 2012: Understanding imaging methods for potential field data. Geophysics, **77**, 1, G13–G24, doi: 10.1190/geo2011-0078.1.

Griffiths D. H., King R. F., 1981: Applied Geophysics for Geologist and Engineers. 2nd ed., Pergamon Press, New York, 230 p.

Guo L., Shi L., Meng X., 2011a: 3D correlation imaging of magnetic total field anomaly and its vertical gradient. J. Geophys. Eng., **8**, 2, 287–293, doi: 10.1088/1742-2132/8/2/013.

Guo L., Meng X., Shi L., 2011b: 3D correlation imaging of the vertical gradient of gravity anomaly. J. Geophys. Eng., **8**, 1, 6–12, doi: 10.1088/1742-2132/8/1/002.

Guo L., Meng, X., Zhang, G., 2014: Three dimensional correlation imaging for total amplitude magnetic anomaly and normalized source strength in the presence of strong remanent magnetization. J. Appl. Geophys., **111**, 121–128, doi: 10.1016/j.jappgeo.2014.10.007.

Hinze W. J., Von Frese R. R. B., Saad A. H., 2013: Gravity and magnetic exploration – Principles, practices, and applications. Cambridge University Press, 525 p.

Klemm R., Klemm D., 2013: Gold and gold mining in Ancient Egypt and Nubia: geoarchaeology of the ancient gold mining sites in the Egyptian and Sudanese Eastern Deserts. Springer, Heidelberg, New York, Dordrecht, London, 664 p.

Li Y., Oldenburg D. W., 1996: 3-D inversion of magnetic data. Geophysics, **61**, 2, 394–408, doi: 10.1190/1.1443968.

Li Y., Oldenburg D. W., 1998: 3-D inversion of gravity data. Geophysics, **63**, 1, 109–119, doi: 10.1190/1.1444302.

Liu G., Yan H., Meng X., Chen Z., 2014: An extension of gravity probability tomography imaging. J. Appl. Geophys., **102**, 62–67, doi: 10.1016/j.jappgeo.2013.12.012.

Mauriello P., Monna D., Patella D., 1998: 3D geoelectric tomography and archeological applications. Geophys. Prospect., **46**, 5, 543–570, doi: 10.1046/j.1365-2478.1998.00102.x.

Mauriello P., Patella D., 1999a: Resistivity anomaly imaging by probability tomography. Geophys. Prospect., **47**, 3, 411–429, doi: 10.1046/j.1365-2478.1999.00137.x.

Maurillo P., Patella D., 1999b: Principles of probability tomography for natural-source electromagnetic induction fields. Geophysics, **64**, 5, 1403–1417, doi: 10.1190/1.1444645.

Maurillo P., Patella D., 2001: Gravity probability tomography: a new tool for buried mass distribution imaging. Geophys. Prospect., **49**, 1, 1–12, doi: 10.1046/j.1365-2478.2001.00234.x.

Maurillo P., Patella D., 2005: Localization of magnetic sources underground by a data adaptive tomographic scanner. arXiv:physics/0511192v2, 1–15, doi: 10.48550/arXiv.physics/0511192.

Mauriello P., Patella D., 2008: Localization of magnetic sources underground by a probability tomography approach. Prog. Electromagn. Res. M, **3**, 27–56, doi: 10.2528/PIERM08050504.

Mohamed H., Mizunaga H., Saibi H., 2020: Computation of geophysical magnetic data caused by a buried 3-D hexahedral prism using the Gauss–Legendre Quadrature Method. Near Surf. Geophys., **18**, 5, 575–588, doi: 10.1002/nsg.12104.

Nabighian M. N., 1972: The analytic signal of two-dimensional magnetic bodies with polygonal cross-section: its properties and use for automated anomaly interpretation. Geophysics, **37**, 3, 507–517, doi: 10.1190/1.1440276.

Patella D., 1997a: Introduction to ground surface self-potential tomography. Geophys. Prospect., **45**, 4, 653–681, doi: 10.1046/j.1365-2478.1997.430277.x.

Patella D., 1997b: Self-potential global tomography including topographic effects. Geophys. Prospect., **45**, 5, 843–863, doi: 10.1046/j.1365-2478.1997.570296.x.

Pilkington M., 1997: 3-D magnetic imaging using conjugate gradients. Geophysics, **62**, 4, 1132–1142, doi: 10.1190/1.1444214.

Saad A. H., 1969: Magnetic properties of ultramafic rocks from Red Mountain, California. Geophysics, **34**, 6, 974–987, doi: 10.1190/1.1440067.

Salem A., Ravat D., 2003: A combined analytic signal and Euler method (AN-EUL) for automatic interpretation of magnetic data. Geophysics, **68**, 6, 1952–196, doi: 10.1190/1.1635049.

Telford W. M., Geldart L. P., Sheriff R. E., 1990: Applied Geophysics. 2nd ed., Cambridge University Press, New York, 770 p.

Thompson D. T., 1982: EULDPH: A new technique for making computer-assisted depth estimates from magnetic data. Geophysics, **47**, 1, 31–37, doi: 10.1190/1.1441278.

Williams N., 2008: Geologically-constrained UBC–GIF gravity and magnetic inversions with examples from the Agnew-Wiluna Greenstone Belt, Western Australia. Ph.D. Thesis, Earth, Ocean and Atmospheric Sciences Department, The University of British Columbia, Vancouver, B.C., doi: 10.14288/1.0052390.

Zhdanov M. S., 2002: Geophysical inverse theory and regularization problems. Methods in Geochemistry and Geophysics series, **36**, Elsevier Science, 633 p.